Evidence of inverse energy cascades in cerebral dynamics

Christian Kerskens*
Trinity College Institute of Neuroscience, Trinity College Dublin, Dublin, Ireland

David López Pérez
Neurocognitive Development Lab and Developmental Psychology Unit,
Faculty of Psychology, University of Warsaw, Warsaw, Poland

Abstract

Brain functions depend on cerebral transport mechanisms which are evidently propelled and regulated throughout the entire brain [1]. It is generally believed that the cardiac pulse wave is the main driving force [2]which, after arrival in the brain, seems to travel effortlessly from the arterial into the venous system without any delay. Paradoxically, the arterial and venous system are not directly connected to allow such a smooth transfer [3]. Instead, cerebral pulsation decays from large scales (arteries) to small scales (capillaries, tissue) [2, 3] in a heart beat. The paradox reverse outflow starting from small scales towards the veins [4] may then only be realized by backward energy cascades, so-called inverse cascades [5]. However, inverse cascades in three dimensions are considered to be a rare phenomenon which, if existing, are most likely accompanied by spontaneously broken mirror-symmetries [6, 7, 8]. Here, we focused on the latter utilizing multiple spin echos (MSE)s [9, 10, 11] to detect symmetry breaking in the human brain at rest. For every heart cycle, we found broken symmetries during the arterial pulsation. From our findings, we conclude a flow cycle separated into two phases. In the first, the arterial pulsation (decaying cascade) injects energy to start reverse flow from tissue level toward the veins (inverse cascade). In the following phase, the outflow continues in the vein while inflow from the arteries flows unhindered into tissue (decaying cascade). This interplay of decaying and inverse cascades explains how the illusive pulse wave traveling through the brain emerges.

Blood flow is commonly considered to be laminar provided that flow is studied in healthy blood vessels. Nevertheless, cerebral dynamics of the entire brain, where inter- and intracellular flows are included, may not meet the criteria for laminar flow. As this is widely disregarded, let us use the following example; water traveling as laminar flow inside an artery at high speed, the freely diffusible water molecules transiting randomly through the vessel wall into the tissue. As this occurs, it looses its layered flow pattern. In addition, the abrupt change of velocity during this transition enforces the turbulent behavior. Consequently, vorticity-induced cascades to smaller scales must exist [12] which in turn matches the anatomically predetermined scales given by arteries, arterioles, capillaries, inter- and intracellular etc. [13] Those anatomical scales also exist in the venous system [3]. Obviously, in a reverse manner because the return flow to venous system undergoes an inverse velocity change from slow to fast. In turbulent systems, this reverse mechanism must entail backward energy cascades to larger scales (inverse cascades). First predicted in 2D [5], inverse cascades in 3D [6] may only be realized if a mirror-symmetry breaking exist which has been proposed as a key mechanism [7]. Only recently, mirror-symmetry breaking has been predicted to exist in active matter, in particular in

*Corresponding author: christian@kerskens.me

bacteria [7, 14, 15, 16].

The brain also contains active matter. And it has a reverse flow starting at small scale. Does then the reserve flow result from 3D inverse cascade involving mirror-symmetry breaking? To answer this question, we used a magnetic resonance imaging (MRI) contrast which shares the need for broken symmetries. So-called multiple spin echos (MSEs) [9, 10, 11] or intermolecular multiple quantum coherences (iMQCs) [17, 18] result from broken spherical symmetries in the non-linear demagnetization field. This asymmetry can be introduced or amplified by gradient fields [9, 11, 17], RF pulses [19], and local field-inhomogeneities and anisotropies [20, 21, 22, 23]. Two radio-frequency (RF) pulses combined with a magnetic field gradient are sufficient to generate MSEs. Consequently, MSEs are present in many MRI sequences, especially in imaging series which are rapidly repeated. There, crusher gradients are added between two acquisitions with the primary intent to dephase any signal that remains from the previous excitation. This is where MSEs come into the game. They appear where the linear single spin echos (SSEs) disappear due to dephasing.

In an imaging series with fast repetitions, single and multiple spin echos will reach a steady state which then, in case of a human brain, will be disturbed by movement and physiological changes. Possible signal alternations which follow from the Bloch equations can be detected in SSEs and MSEs. They conclude changes of the magnetization vector $\vec{M}_0$ which can be changed by brain movement, flow, and to some extent by diffusion and changes in T_1, T_2 and T_2^* relaxation. In contrast, symmetry changes which do not influence relaxation are exclusive to MSEs.

I. Results

In our experiments, we used a conventional single-slice gradient-echo echo planar imaging (GE-EPI) series with a short repetition time (TR) instead of a dedicated MSE sequence. While this had some limitations towards the variability of some sequence parameters, it allowed a simultaneous acquisition of SSE and MSE. With this sequence, we found predominate alternations with the cardiac frequency in brain tissue. In each cardiac cycle, we observed a period which varied in length between 150 and 420 ms showing a pattern as plotted in Figure 1A.

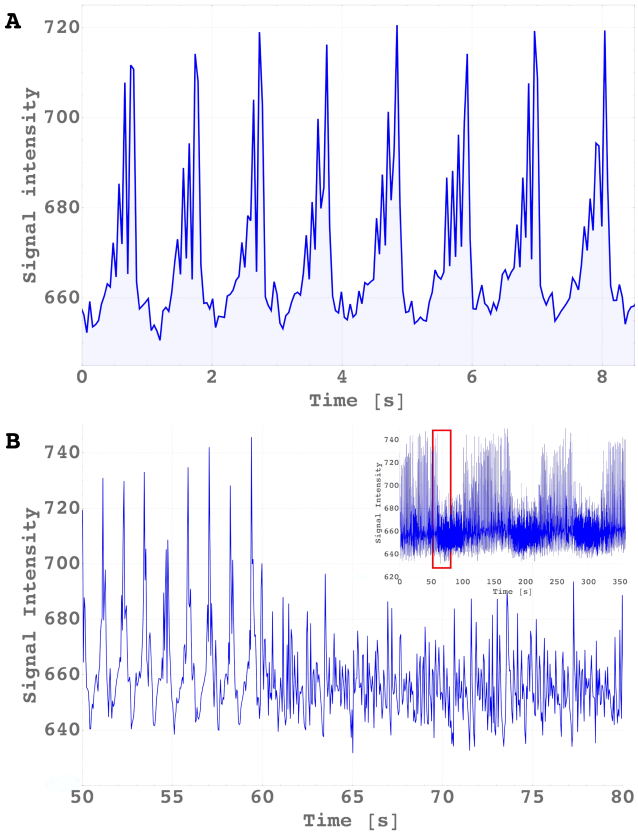

Figure 1: *A: Whole-slice averaged signal time course (selected by a mask) during 8 heart cycles. Subject had extra head fixation and was instructed to breath-hold during the period.* ***B:*** *Whole-slice averaged signal time course during normal breathing first. At 60 s, the subject was instructed to hyperventilate. The inlet shows the total time course with 3 hyperventilation periods and the selected time interval in red.*

It was characterized by a signal increase of up to 15 % and it was modulated by an alternating zigzag. The start of the period depended

strongly on the head's mobility/fixation. The pattern as shown in Figure 1A was achieved using additional cushions inside the coil and by breath-holding (without taking a deep breath). Under normal condition, the zigzags usually only contain two or three maxima as shown in Figure 1B during the first 10s from 50s to 60s. At 60s, the volunteer was instructed to hyperventilate with the result that the pattern immediately disappeared. In steady conditions, the pattern always appeared during the arterial inflow phase. The abrupt end of the zigzag pattern were coincident with the end-phase of the arterial pulse as shown inFigure 2A and the rise of venous outflow as demonstrated in Figure 2B.

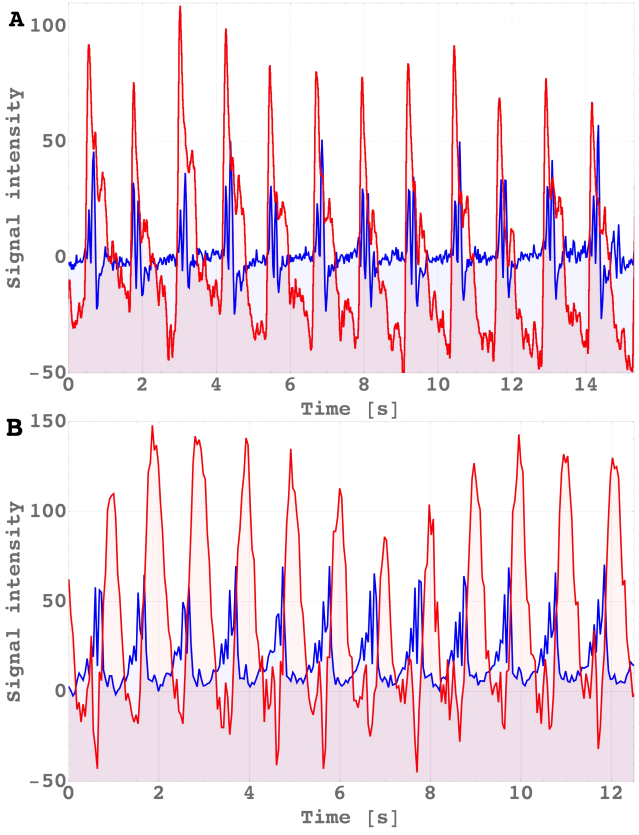

Figure 2: *Signal time course (Blue) during 12 heart cycles compared with **A**: Simultaneous oximeter reading of a finger (Red) and **B**: Signal time course (Red) of a vein.*

We located the zigzag pattern in tissue over the entire brain tissue except in areas which are known to be prone to motion like the periventricular area [24]. Regions like skull, ventricle etc and in the attached test tubes showed no zigzag pattern.

Otherwise, we found that the zigzag pattern, including the sudden end, could be restored while being averaged over the whole imaging slice Figure 1A. For investigation of the underlying contrast mechanism, we varied the following sequence parameters using the averaged signal : (a) the slice angulation, (b) the off-resonance frequency of the saturation pulses, (c) the flip angle (FA) with saturation pulses, and (d) the flip angle (FA) without saturation pulses. For (a), we found the angle dependency of the demagnetization field as shown inFigure 3A where φ is the angle between the slice gradient and the main magnet field. The plot represents the fitted function $|(3 \cdot cos^2[\varphi_{cor}] - 1)|$ with $R^2 = 0.9958$ where φ_{cor} takes additional gradients in read direction into account. For (b), we found a typical magnetization transfer contrast (MTC) change for the baseline signal which depended on the off-resonance frequency (Figure 3B, left-hand side). In contrast, the zigzag intensity showed no significant changes in the same frequency range (Figure 3B, right-hand side). For (c), we found a maximum peak intensity at 45° (Figure 3 C). It followed the predicted signal course [25] in a range from 20 to 60° ($R^2 = 0.9964$). For (d), we could extend our observation to 90° where we found a flat plateau following an initial signal increase. In comparison, with (c) the signal was lower from 25° onward as shown in Figure 3C.

II. Discussion

From our results, we conclude that the observed zigzag pattern is generated by at least two RF pulses and by the demagnetization field which produced the angle dependency in Figure 3A.

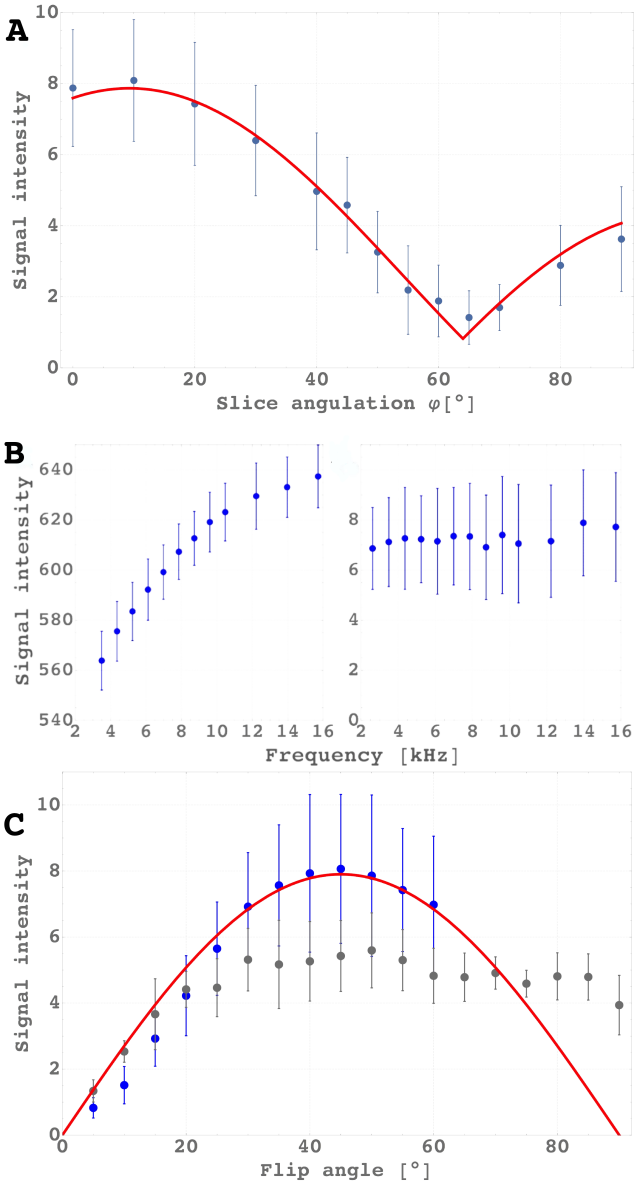

Figure 3: *A: Signal intensity plotted against the slice gradient angulation φ in respect to the magnetic main field. The function was fitted to the data shown as red line.* ***B****: Signal intensity plotted against the frequency offset of the saturation slices of the averaged baseline signal (left) and averaged signal of cardiac pattern (right).* ***C****: Whole-slice averaged signal time course plotted against flip angle variation with saturation pulses (Blue) and without (Grey). IZQC prediction plotted in Red.*

They are the essential ingredients for MSEs. The sequence layout suggests an intermolecular zero-quantum coherence (iZQC) mechanism [26]. In the case with the saturation pulses, we could confirm iZQC for the zigzag pattern because it showed the remarkably immunity for MTC [27] and a flip angle dependency with a maximum at 45° [25]. Without the saturation pulses, we found a mixture of all quantum orders n which explains the destructive coherences (signal plateau from 30°onward) [28] dephasing the signal at higher flip angle. The generation of higher quantum orders underpins that the applied magnetic field gradients are not alone responsible for the broken spherical symmetry. Indeed, from the temporal character of signal it follows that the broken symmetry originates in the tissue. At the magic angle, the cardiac pattern disappeared completely which leads us to exclude any SSE component. With this we can exclude that the signal was generated by flow or movement, relaxation, field inhomogeneities or other multiple RF effects like stimulated echos. Movement which would be the most expected signal source could also be excluded due to the high movement sensibility of iZQC as demonstrated in the hyperventilation. The fact, that the signal was generated in the tissue only, rules out further MRI artifacts. The timing of zigzag suggests broken symmetries coincident with the desired inverse cascades which are always accompanied by decaying cascades at larger scale (arterial pulsation). The predominance of the alternating zigzag even at signals averaged over the whole slice, suggest a global symmetry breaking. In a further study, we have shown that the global character is not a given fact but declines in healthy aging and disappears completely with cognitive impairment [29].

III. Methods

40 subjects (between 18 and 46 years old) were scanned in a 3.0 T Philips whole-body MRI scanner (Philips, The Netherlands) operated with a 32-channel array receiver coil. Imaging protocols using standard single-shot GE EPI sequence

were approved by the Trinity College School of Medicine Research Ethics Committee.
Initial experiments were carried out to establish a protocol that could deliver stable cardiac related signals over a range of subjects. Initially, test tubes with a water solution (1000ml demineralized water contained 770 mg $CuSO_4 5H_2O$, 1 ml Arquad (AkzoNobel), 0.15 ml H_2SO_4-(0.1 N) were positioned closely to the head for reference signals. The finalized parameters of the GE-EPI sequence were as follows: FA = 45, TR = 45 ms and the TE = 5 ms with a voxel size was 3.5 x 3.5 x 3.5 mm, matrix size was 64x64, SENSE factor 3, bandwidth readout direction was 2148 Hz.

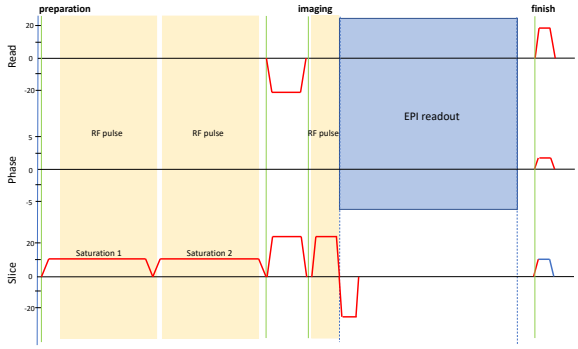

Figure 4: *Gradient scheme of the EPI sequence with two saturation pulse.*

Figure 4 shows the gradient scheme. Saturation gradients had an time integral (length x strength) of $Gt_{sat} = 5.1$ ms x 6.25 mT/m, the crusher gradients in read and slice direction of $Gt_{cru} = 1.3$ ms x 25 mT/m, the slice rephase gradient of $Gt_{sr} = 0.65$ ms x 25 mT/m, the slice termination gradient of $Gt_{st} = 0.65$ ms x 15 mT/m, and the total read dephase after EPI readout gradient of $Gt_{rt} = 0.65$ ms/ x 22.5 mT/m. The angle between magnet field and gradient field was then

$$\begin{aligned} \varphi_{cor} &= \varphi - \tan^{-1}\left[\frac{Gt_{cru} - Gt_{rt}}{2Gt_{sat} + Gt_{cru} + Gt_{st}}\right] \\ &= \varphi - 9.6^{\circ} \end{aligned}$$

where φ is the slice angulation. The imaging slice was set coronal above the ventricle. In addition, two saturation slices of 5 mm (15mm above and 20mm below) in thickness were placed parallel to the imaged slice. The following alternation (each with 1000 repetitions in five participants) were carried out, (a) slice angulation starting from coronal 0°to axial 90°in the steps as [0, 10, 20, 30, 40, 45, 50, 55, 60, 65, 70, 80, 90], (b) the distance of the REST slabs were varied between 0.8 mm and 50 mm to alter the off-resonance frequency. The off-resonance frequencies were [2.62, 3.49, 4.36, 5.23, 6.11, 6.98, 7.84, 8.73, 9.60, 10.47, 12.22, 13.96, 15.71, 17.45] kHz, (c) Flip angle was varied for the case with saturation pulses from 5° to 60° in steps of 5°(60°was the power limit by the specific absorption rate (SAR)) and without saturation pulses from 5°to 90° in steps of 5°, (d) 9 slices were acquired at different positions, with each slice matching from bottom to the top the position of those acquired in the anatomical scan. In four participants, we examined the motion sensitivity where we fixated the head with multiple cushions. During indicated intervals the subjects were asked to stop breathing for 20 s or to hyperventilate for 40 s. Finally, anatomical MRI images in all studies included a high-resolution sagittal, T1-weighted MP-RAGE (TR = 2.1 s, TE = 3.93 ms, flip angle = 7).
Data were processed with Matlab 2014a (http://www.mathworks.co.uk/). Rescaling was applied to all data sets before any analysis using the MR vendor's instructions. Average time series were visually inspected in search for irregularities which were manually removed from the analysis leaving the rest of the time series unaltered. Manual segmentation was used to create a mask to remove cerebral spinal fluid (CSF) contributions. The first 100 scans were removed to avoid signal saturation effects. The manual segmentation of the masks was eroded to avoid partial volume effects at the edges. The cardiac signal and baseline detection was based on the method proposed in Gomes and Pereira [30]. Final data presentation was carried with Mathematica (Wolfram Research, Champaign, Illinois).

Authors' contributions

D.L.P. and C.K. performed experiments, D.L.P. analyzed the data, C.K. designed the research and wrote the paper.

Acknowledgments

We would like to thank S. Joseph for carrying out the imaging protocols for our participants, R. Fallon for reading the manuscript, and Science Foundation Ireland for supporting D.L.P. from 2011-2015 (SFI-11/RFP.1/NES/3051)

References

[1] Lassen, N. A. Cerebral blood flow and oxygen consumption in man. *Physiological Reviews* **39**, 183–238 (1959).

[2] Wagshul, M. E., Eide, P. K. & Madsen, J. R. The pulsating brain: A review of experimental and clinical studies of intracranial pulsatility. *Fluids and Barriers of the CNS* **8**, 5 (2011).

[3] Nedergaard, M. Garbage truck of the brain. *Science* **340**, 1529–1530 (2013).

[4] Iliff, J. J. *et al.* Cerebral arterial pulsation drives paravascular csf-interstitial fluid exchange in the murine brain. *The Journal of Neuroscience* **33**, 18190–18199 (2013).

[5] Kraichnan, R. H. Helical turbulence and absolute equilibrium. *Journal of Fluid Mechanics* **59**, 745–752 (1973). URL 10.1017/S0022112073001837.

[6] Moffatt, H. K. The degree of knottedness of tangled vortex lines. *Journal of Fluid Mechanics* **35**, 117–129 (1969). URL 10.1017/S0022112069000991.

[7] Biferale, L., Musacchio, S. & Toschi, F. Inverse energy cascade in three-dimensional isotropic turbulence. *Phys. Rev. Lett.* **108**, 164501 (2012). URL 10.1103/PhysRevLett.108.164501;https://link.aps.org/doi/10.1103/PhysRevLett.108.164501.

[8] Slomka, J. & Dunkel, J. Spontaneous mirror-symmetry breaking induces inverse energy cascade in 3d active fluids (article) author. *Proceedings of the National Academy of Sciences* (2017).

[9] Deville, G., Bernier, M. & Delrieux, J. M. Nmr multiple echoes observed in solid 3he. *Physical Review B* (1979).

[10] Eska, G., Willers, H. G., Amend, B. & Wiedemann, C. Spin echo experiments in superfluid 3he. *Physica B+ C* (1981).

[11] Bowtell, R., Bowley, R. M. & Glover, P. Multiple spin echoes in liquids in a high magnetic field. *Journal of Magnetic Resonance (1969)* **88**, 643–651 (1990).

[12] Kolmogorov, A. N. The local structure of turbulence in incompressible viscous fluid for very large reynolds numbers. In *Dokl. Akad. Nauk SSSR*, vol. 30, 299–303 (1941).

[13] Hladky, S. B. & Barrand, M. A. Mechanisms of fluid movement into, through and out of the brain: evaluation of the evidence. *Fluids and Barriers of the CNS* **11**, 26 (2014).

[14] Woodhouse, F. G. & Goldstein, R. E. Cytoplasmic streaming in plant cells emerges naturally by microfilament self-organization. *Proceedings of the National Academy of Sciences* **110**, 14132–14137 (2013).

[15] Wioland, H., Woodhouse, F. G., Dunkel, J., Kessler, J. O. & Goldstein, R. E. Confinement stabilizes a bacterial suspension into a spiral vortex. *Phys. Rev. Lett.* **110**, 268102 (2013). URL 10.1103/PhysRevLett.110.268102;https://link.aps.org/doi/10.1103/PhysRevLett.110.268102.

[16] Sokolov, A. & Aranson, I. S. Physical properties of collective motion in suspensions of bacteria. *Phys. Rev. Lett.* **109**, 248109 (2012). URL 10.1103/PhysRevLett.109.248109;https://link.aps.org/doi/10.1103/PhysRevLett.109.248109.

[17] Warren, W. S., Richter, W., Andreotti, A. H. & Farmer, B. T. Generation of impossible cross-peaks between bulk water and biomolecules in solution nmr. *Science* **262**, 2005–2009 (1993).

[18] Minot, E. D., Callaghan, P. T. & Kaplan, N. Multiple echoes, multiple quantum coherence, and the dipolar field: Demonstrating the significance of higher order terms in the equilibrium density matrix. *Journal of Magnetic Resonance* **140**, 200–205 (1999).

[19] Jerschow, A. Multiple echoes initiated by a single radio frequency pulse in nmr. *Chemical Physics Letters* **296**, 466–470 (1998).

[20] Bouchard, L. S., Rizi, R. & Warren, W. Magnetization structure contrast based on intermolecular multiple-quantum coherences. *Magn Reson Med* **48**, 973–979 (2002).

[21] Bowtell, R., Gutteridge, S. & Ramanathan, C. Imaging the long-range dipolar field in structured liquid state samples. *Journal of Magnetic Resonance* **150**, 147–155 (2001).

[22] Capuani, S., Alesiani, M., Branca, R. T. & Maraviglia, B. New openings for porous systems research from intermolecular double-quantum nmr. *Solid State Nuclear Magnetic Resonance* **25**, 153–159 (2004).

[23] Bouchard, L. S., Wehrli, F. W., Chin, C. L. & Warren, S. W. Structural anisotropy and internal magnetic fields in trabecular bone: Coupling solution and solid dipolar interactions. *Journal of Magnetic Resonance* **176**, 27–36 (2005).

[24] Nunes, R., Jezzard, P. & Clare, S. Investigations on the efficiency of cardiac-gated methods for the acquisition of diffusion-weighted images. *J Magn Reson* **177**, 102–110 (2005).

[25] Zhong, C., Shaokuan, Z. & Jianhui, Z. Optimal rf flip angles for multiple spin-echoes and imqcs of different orders with the crazed pulse sequence. *Chemical Physics Letters* **347**, 143–148 (2001). URL `https://doi.org/10.1016/S0009-2614(01)01042-9;http://www.sciencedirect.com/science/article/pii/S0009261401010429`.

[26] Warren, W. S. *et al.* Mr imaging contrast enhancement based on intermolecular zero quantum coherences. *Science* **281**, 247–251 (1998).

[27] Uzi, E. & Gil, N. Enhancement of magnetization transfer effects by inter-molecular multiple quantum filtered nmr. *Journal of Magnetic Resonance* **190**, 149–153 (2008). URL `https://doi.org/10.1016/j.jmr.2007.09.017;http://www.sciencedirect.com/science/article/pii/S109078070700300X`.

[28] Baum, J., Munowitz, M., Garroway, A. N. & Pines, A. Multiple-quantum dynamics in solid state nmr. *Multiple-quantum dynamics in solid state NMR,J. Chem. Phys. 83, 2015 (1985)* (1985).

[29] Perez, D. L., Bokde, A. & Kerskens, C. Complexity and chaos in intermolecular zero-quantum coherence fluctuations in the ageing brain. *under preparation* .

[30] Gomes, E. F., Jorge, A. M. & Azevedo, P. J. Classifying heart sounds using peak location for segmentation and feature construction. In *Proceedings of the International C* Conference on Computer Science and Software Engineering*, 23–30 (ACM, 2013).